Variations in Strength and Slip Rate Along the San Andreas Fault System

Craig H. Jones and Steven G. Wesnousky

Convergence across the San Andreas fault (SAF) system is partitioned between strike-slip motion on the vertical SAF and oblique-slip motion on parallel dip-slip faults, as illustrated by the recent magnitude M_s = 6.0 Palm Springs, M_s = 6.7 Coalinga, and M_s = 7.1 Loma Prieta earthquakes. If the partitioning of slip minimizes the work done against friction, the direction of slip during these recent earthquakes depends primarily on fault dip and indicates that the normal stress coefficient and frictional coefficient (μ) vary among the faults. Additionally, accounting for the active dip-slip faults reduces estimates of fault slip rates along the vertical trace of the SAF by about 50 percent in the Loma Prieta and 100 percent in the North Palm Springs segments.

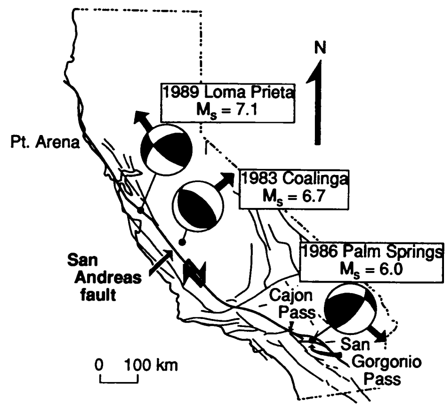

Fig. 1. Focal mechanisms, magnitudes, and horizontal projection of coseismic slip vectors (solid arrows) for large oblique-slip earthquakes that have recently occurred adjacent to the mapped trace of the SAF.

The San Andreas fault (SAF) system is characterized by the repeated occurrence of large strike-slip offsets. Yet during the last decade a number of moderate to large thrust and oblique-slip earthquakes have occurred on faults adjacent to the mapped trace of the SAF. These oblique-slip faults are thought to accommodate oblique convergence along the plate boundary [for example (*1*, *2*)]. The occurrence of slip partitioning along major convergent plate boundaries has long been known (*3*), but relatively little work has been directed toward understanding partitioning along strike-slip fault zones and, principally, the SAF. In this report, we discuss the factors that control slip partitioning along the SAF zone.

We focus on the magnitude M_s = 6.0 Palm Springs earthquake of 8 July 1986 (*4*, *5*), the M_s = 6.7 Coalinga earthquake of 2 May 1983 (*6*), and the M_s = 7.1 Loma Prieta earthquake of 17 October 1989 (*7*)—the largest oblique slip earthquakes to have occurred along the SAF during the past decade (Fig. 1). The strike of the fault plane for each event is nearly parallel to that of the adjacent SAF. In contrast, the slip vectors differ greatly among the three events. Slip during the Palm Springs and Loma Prieta earthquakes was approximately parallel to the SAF whereas slip during the Coalinga earthquake was almost perpendicular to it.

In examining the cause for these differences, we initially assume that the amount of slip partitioning between thrust and strike-slip motion will be that minimizing the work per unit convergence across the fault zone (Fig. 2) (*8*). Slip is allowed to have any rake on the dipping fault but only strike slip on the strike-slip fault. We examine two possible end-member models of how plate motions might be expressed in this system (Fig. 3). In the first (*9*), horizontal motion on the two faults equals the plate motion; this requires that the footwall extend as the surface passes through the hinge line (Fig. 3A). In the second, the footwall moves with constant speed both far from the thrust fault and under it (Fig. 3B). Because the velocity is parallel to the thrust plane, the horizontal component of the motion of the footwall relative to the stable plate does not equal the far-field motion. In the first model, continuity of the footwall is ignored whereas, in the second, any deformation of the footwall at the thrust fault is ignored.

We determine the value of ψ (the azimuth of slip on the thrust) that minimizes the work (W) done for a unit of convergence along a unit length of the boundary. More specifically, we determine the value of ψ that satisfies $\partial W/\partial\psi = 0$. We can express W as

$$W = W_S + W_T + W_D + W_G \qquad (1)$$

where W_S and W_T are the work done against friction on the strike-slip and thrust faults, respectively, W_D is the work done in anelastic deformation, and W_G is the work done against gravity. Because the last two terms of Eq. 1 depend mostly on the thrust-normal convergence rate, which is independent of ψ, we ignore these terms (*10*). The first two terms can be considered to be of the form $\mu\ \sigma\ |v|\ A$, where μ is the coefficient of frictional resistance, σ is the deviatoric normal stress in the fault, v is the slip, and A is the area of the fault plane.

To differentiate Eq. 1, we must know how normal stresses on the two faults vary with ψ. We assume that one principal stress is vertical, in which case

$$(\sigma_t - \sigma_z) = (\sigma_s - \sigma_z)\sin^2\Delta \qquad (2)$$

where σ is stress and the subscripts denote normal stresses on the thrust (t), strike-slip (s), and horizontal (z) planes (Fig. 3C). From standard stress tensor identities, $\sigma_s = \sigma_H + \sigma_h - \sigma_x$, where the three right-hand terms are the maximum (H) and minimum (h) principal horizontal stresses and the stress on the plane perpendicular to the strike (x) of both faults (Fig. 3C). We assume that σ_x does not depend on ψ because our model cannot absorb strain parallel to the x-axis. Furthermore, from the assumption that the sum of $\sigma_H + \sigma_h$ is unchanged by changes in ψ it may be inferred that σ_s and, from Eq. 2, σ_t are also independent of ψ.

Center for Neotectonic Studies, University of Nevada, Reno, NV 89557.

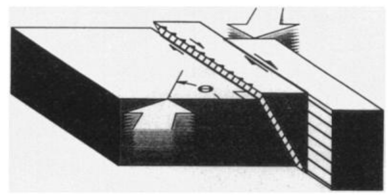

Fig. 2. Oblique convergence oriented at an angle θ to the normal of a plate boundary or fault zone is commonly accommodated by slip partitioning: a combination of oblique dip-slip motion on a dipping fault plane and strike-slip motion on an adjacent vertical fault plane.

We may now evaluate Eq. 1 by determining the slip rates in terms of ψ, Δ, and θ (Fig. 3, A and B). For the second kinematic model (Fig. 3B):

$$v_s = V\,(\sin\theta - \cos\theta\cos\Delta\tan\psi) \qquad (3A)$$

$$v_t = v_{th}\,(1 + \cos^2\psi\tan^2\Delta)^{1/2} = V\,\frac{\cos\theta\cos\Delta}{\cos\psi}\,(1 + \cos^2\psi\tan^2\Delta)^{1/2} \qquad (3B)$$

For the first case (Fig. 3A) the $\cos\Delta$ term drops from Eqs. 3A and 3B. Equation 3A implies that the slip rate on a planar strike-slip fault varies depending on the dip of the adjacent thrust fault and the rake of the slip vector on the thrust plane. Differentiation of W with respect to ψ then yields

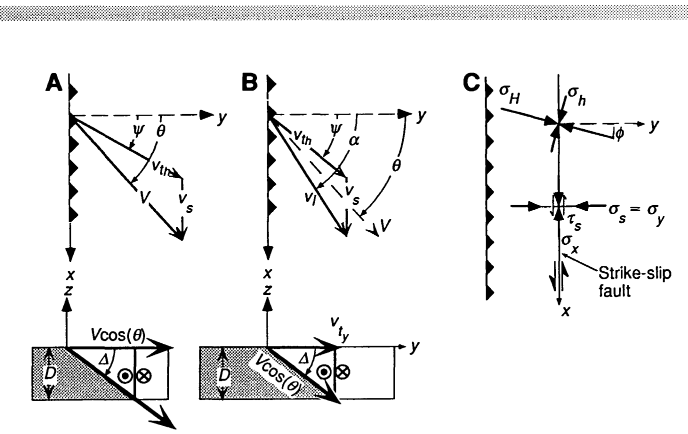

Fig. 3. (**A** and **B**) Map and cross section of two limiting models for the partitioning of slip as in Fig. 2. Dip of oblique slip fault is Δ. Far-field horizontal plate motion V is oriented at angle θ to the normal of the parallel faults. Vector v_{th} is the horizontal projection of the slip vector on the dipping plane and is oriented at angle ψ to the normal of the fault strike. Vector v_s is the component of strike-slip motion accommodated by the vertical strike-slip fault. It is assumed in (A) that the horizontal component of motion across the paired fault system equals V. In (B), it is assumed that, much like a conveyor belt, the speed of motion along the footwall is equal to V. A consequence is that the local horizontal component of motion (v_l) along the dipping plane will be rotated to angle $\alpha = \tan^{-1}(\tan\theta/\cos\Delta)$. (**C**) Notation used for stress orientations: top, orientation of principal horizontal stresses ($\sigma_H > \sigma_h$); bottom, normal (σ) and shear (τ) stresses resolved in the coordinate system of the strike-slip fault.

$$\frac{\partial W}{\partial \psi} = \mu_s \sigma_s D \frac{\partial |v_s|}{\partial \psi} + \mu_t \sigma_t \frac{D}{\sin\Delta} \frac{\partial |v_t|}{\partial \psi} \quad (4)$$

We can set this to zero and then use Eq. 3 to find that the ratio of the strength of the strike-slip fault to that of the thrust fault, R, depends solely on ψ and Δ:

$$R \equiv \frac{\mu_s \sigma_s}{\mu_t \sigma_t} = \frac{\sin\psi}{\sin\Delta(1 + \cos^2\psi \tan^2\Delta)^{1/2}} \quad (5)$$

where $\theta > \psi$ for the first case (Fig. 3A) and $\alpha > \psi$ for the second (Fig. 3B) (*11*).

We can calculate a uniform stress field that is compatible with our kinematic model by assuming (i) that the shear stresses on the two fault planes must parallel the observed slip vectors and (ii) that there is no shear on a horizontal plane. The assumptions permit us to estimate the relative magnitude of shear and normal stresses on the faults for both cases in Fig. 3.

Assume that σ_H is oriented at an angle ϕ clockwise from the normal to the two faults (Fig. 3C). By deriving the shear stress on the thrust fault and requiring it to parallel the slip vector, it can be shown that

$$S \equiv \frac{\sigma_H - \sigma_z}{\sigma_H - \sigma_h} = \sin^2\phi + \frac{\sin 2\phi}{2\tan\zeta} \quad (6)$$

where $\tan\zeta \equiv \tan\psi \cos^2\Delta$ (*12*). Note that $S > 1$ is equivalent to $\sigma_z = \sigma_3$, $0 < S < 1$ is equivalent to $\sigma_z = \sigma_2$, and $S < 0$ implies that $\sigma_z = \sigma_1$, where σ_1 is the most compressive principal stress. Thus there is a stress field for any value of ϕ that will satisfy the requirement that the shear stress resolved on the two faults parallel the observed slip vectors.

The ratio of the magnitude of the shear stresses may also be obtained from the model. Doing so, it is evident that the strength of a fault will not be solely a function of ϕ but also the stress difference $\sigma_H - \sigma_h$.

$$\tau_s = \frac{1}{2} \sin 2\phi \, (\sigma_H - \sigma_h) \quad (7A)$$

$$\tau_t = \frac{1}{2}(\sigma_H - \sigma_h) \, [\sin^2\Delta \sin^2 2\phi + \sin^2 2\Delta \, (\sin^2\phi - S)^2]^{1/2} \quad (7B)$$

The ratio of stresses τ_s/τ_t reduces to R [(*13*) Eq. 5], once again revealing that R is independent of the orientation of the principal stress or the overall slip direction. Thus, constraining the orientation of the principal stresses does not constrain the relative strengths of the strike-slip and thrust planes.

For any given value of R, the predicted value of ψ (Eq. 5) (*11*) strongly depends on the dip angle Δ of the thrust plane. It is apparent that the extremely low value of ψ observed for Coalinga is mostly due to the shallow dip angle of the fault (Fig. 4). In contrast, the larger values of ψ observed for the Loma Prieta and North Palm Springs earthquakes reflect the steeper dips of their respective faults. However, withstanding the strong dependence on dip, the data indicate that R varies along strike of the SAF system.

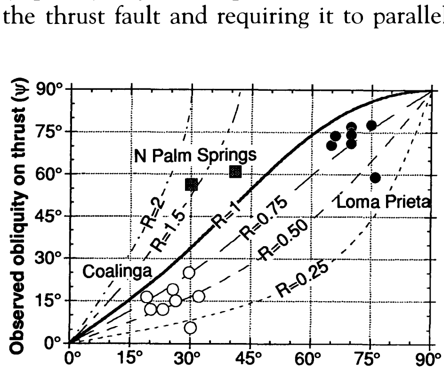

Fig. 4. Dip angle of thrust versus observed slip azimuth on thrust, with contours of constant values of R from Eq. 5. Observed values of dip and rake determined by different investigators for the Coalinga (*6*) (open circles), North Palm Springs (*4, 5*) (squares), and Loma Prieta (*7*) (solid circles) earthquakes are denoted.

Focal mechanism parameters for the Coalinga earthquake consistently plot beneath the line $R = 0.75$ (Fig. 4), whereas parameters for the Loma Prieta and Palm Springs events plot above the line. Both the North Palm Springs and Loma Prieta earthquakes occurred along segments of the SAF that strike at significantly oblique angles to the predicted relative plate motion vector. Indeed, our observations indicate that R decreases with increasing θ (Figs. 3 and 5). This relation suggests normal stress on the strike-slip fault must increase more than on the thrust fault as the predicted plate motion vector becomes more oblique to the strike of the SAF. We examine this possibility by calculating σ_s/σ_z for these earthquakes.

Combining Eqs. 5 and 2, we find that

$$R = \frac{\mu_s}{\mu_t} \frac{1}{\sin^2\Delta + \frac{\sigma_z}{\sigma_s}\cos^2\Delta} \quad (8A)$$

$$\frac{\sigma_s}{\sigma_z} = \frac{\cos^2\Delta}{\frac{\mu_s}{\mu_t R} - \sin^2\Delta} \quad (8B)$$

$$\frac{\sigma_t}{\sigma_z} = \frac{\cos^2\Delta}{1 - \frac{\mu_t}{\mu_s} R \sin^2\Delta} \quad (8C)$$

First consider that the observed variations in R are due solely to variations in normal stresses, that is, μ_s/μ_t is constant. Using Eq. 8B we may specify a value of μ_s/μ_t and then calculate σ_s/σ_z for each earthquake using estimates of R from Fig. 4 (Fig. 6).

Without additional constraints, it appears from Fig. 6 that variations in normal stresses might alone explain the observed variations in R. For instance, for $\mu_s/\mu_t = 1$, σ_s/σ_z equals about 0.5 to 0.6 for the Coalinga earthquake (Fig. 6). However, values of σ_s/σ_z greater than about 4 would lie outside

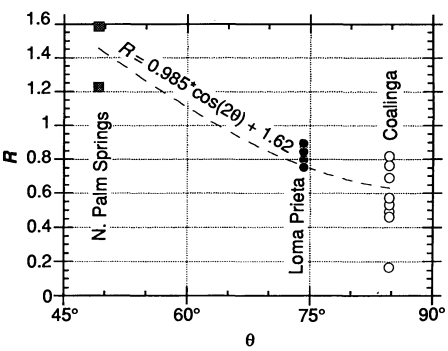

Fig. 5. Computed values of R versus θ (*28*) for the North Palm Springs, Coalinga, and Loma Prieta sections of the SAF without any Basin and Range motion. Regression line of R versus $\cos 2\theta$ is shown for reference.

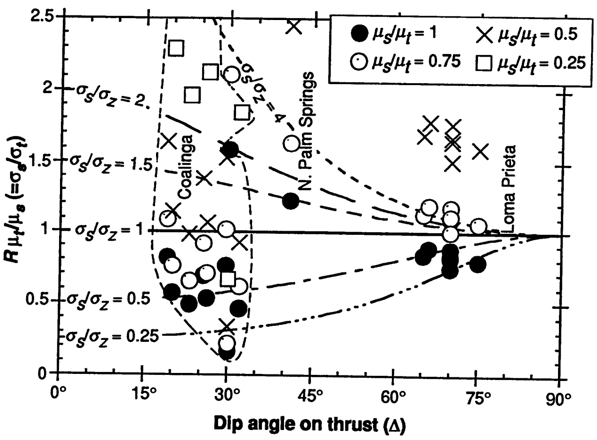

Fig. 6. Dip angle versus R μ_t/μ_s (= σ_s/σ_t) with lines of constant normal stress on the strike-slip fault (σ_s/σ_z). Data from (*4–7*) plotted for different assumed values of μ_s/μ_t. Values of $\sigma_s/\sigma_z \gtrsim 4$ lie outside the stability field predicted from Byerlee's Law, and $\sigma_s/\sigma_z < 1$ implies an extensional stress field if ϕ is small, for example, at Coalinga (ϕ = 6°). The combination of these two constraints precludes a single value of μ_s/μ_t from fitting both the Coalinga and Loma Prieta observations.

the stability field inferred from Byerlee's law (*14*). Thus we infer that $\mu_s/\mu_t > 0.75$ from the Loma Prieta data. Such a constraint then implies that $\sigma_s/\sigma_z < 1$ at Coalinga. We can directly derive the expression for σ_s/σ_z by using the notation in Fig. 3C:

$$\frac{\sigma_s}{\sigma_z} = 1 + \frac{(\sigma_H - \sigma_h)}{\sigma_z}(S - \sin^2\phi) \quad (9)$$

Thus for $\sigma_s/\sigma_z < 1$, it is necessary that $S < \sin^2\phi$. But observations show that σ_H at Coalinga is oriented about 6° from the normal to the SAF (*15*); using ϕ = 6° and observed focal parameters for Coalinga, we estimate that S from Eq. 6 is between 0.4 and 0.65. Thus $\sigma_s/\sigma_z > 1$, and so we suggest from Fig. 6 that $\mu_s/\mu_t < 0.5$ at Coalinga. This lower value of μ_s/μ_t may reflect that Coalinga is located adjacent to the creeping section of the SAF.

The alternative hypothesis, that σ_s/σ_z is constant, is usually possible because we lack constraints on μ_s/μ_t. Thus we can only place a minimum bound on variations of μ_s/μ_t.

Because it is difficult to fit R for both the Loma Prieta and Coalinga earthquakes with a single ratio μ_s/μ_t, we suggest that variations in R reflect variations both in the magnitude of the normal stresses on the SAF and in μ, either between the thrust faults or along the strike of the SAF. If we minimize the variations in μ_s/μ_t by setting it to 0.5 for Coalinga and 0.75 for Loma Prieta, the estimates of σ_s/σ_z are about 1 and 4, respectively. This result seems compatible with the correlation between R and θ, for we expect that σ_s (and, by Eq. 8, σ_s/σ_t) increases as θ decreases. Similarly, μ_s might be high in bends along the SAF.

The partitioning of slip requires that slip rate varies along the SAF (Fig. 7). Earthquake repeat times T along given sections of fault are commonly estimated by dividing the coseismic slip u expected to occur during future ruptures by the estimated fault slip rate $\dot{u}$. Because estimates of T along one section of a fault are commonly determined from estimates of slip rate along other sections (*16*), documenting variations in slip rate resulting from partitioning is important. Our calculations, based on the geometry of Fig. 3B, maximize the estimate of v_s and minimize that of v_t.

Prentice (*17*) placed a maximum Holocene slip rate across the SAF system of about 25 mm/year near Point Arena, California, which we assume is characteristic south to the latitude of the Loma Prieta earthquake, where the value of θ is 74° (*18*). Thus from Eq. 3A, the slip rate on the vertical SAF is about 0.7 · 25 mm/year = 18 mm/year. Strike-slip offset during the last major rupture along this fault section in 1906 was ~2.5 m (*16*). The T for this section is thus 2.5 m/18 mm/year ≈ 140 years. The same approach can be used to estimate the T of Loma Prieta earthquakes. Coseismic displacement during the Loma Prieta earthquake was about 2 m (*19*). The slip rate on that fault from Eq. 3B equals about 0.45 · 25 mm/year = 11.5 mm/year. Thus, the T of similarly sized events is ~180 years, similar to the frequency of rupture along the main trace of the SAF. This conclusion also requires that interseismic subsidence (*20*) reduces the coseismic uplift of the shoreline terraces observed for the Loma Prieta earthquake (*21*).

In contrast, the amount of slip accommodated by Coalinga-type earthquakes must be small compared to that on the adjacent SAF. The slip rate of the SAF is approximately 33 mm/year immediately to the north and south and through the Coalinga section (*22*), and θ is about 80° to 85°. Assuming that V = 35 mm/year, we calculate that the total slip rate along the Coalinga thrust fault is about 10 to 20% of that along the SAF, or about 3 to 7 mm/year. Dividing the coseismic slip at a depth of 3.5 m during the Coalinga earthquake (*23*) by 3 to 7 mm/year produces a T of 500 to 1000 years.

Farther to the south, the relatively simple strand of the SAF system within Cajon Pass accommodates about 25 mm/year of plate motion (*24*)—a rate that we infer extends southeast to San Gorgonio Pass. The slip azimuth for the North Palm Springs event strikes near parallel to the predicted plate motion vector ($\theta \approx \psi$). Use of Eq. 3 thus predicts that the entire motion can be accommodated by earthquakes of orientation and slip azimuth similar to the North Palm Springs event and that the vertical trace of the SAF is virtually inactive. This result is supported by both the lack of neotectonic expression of the SAF through the San Gorgonio Pass region (*25, 26*) and the largest values of R that we inferred along the SAF (Fig. 4). Given that estimates of coseismic slip were about 35 cm (*4*) during the event, we should expect a relatively frequent occurrence of such events (14 years), a frequency not observed historically. Because this event is the smallest of those we have examined, most likely slip along this dipping fault occurs primarily during much larger earthquakes, as can be inferred from the significant thrust scarps in San Gorgonio Pass (*28*), which parallel the strike of the inferred fault plane of the North Palm Springs earthquake.

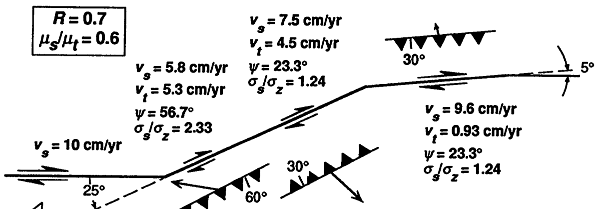

Fig. 7. Schematic illustration of variation in slip rate that will result along a strike-slip fault system when oblique slip is partitioned between strike-slip motion on the main fault and oblique dip-slip motion on adjacent thrust systems (barbed lines). It is assumed that horizontal motion across the fault system (large open arrows) is 10 cm/year parallel to the leftmost segment of the fault. The velocity of motion along the vertical strike-slip fault and adjacent thrust faults, the angle ψ between the horizontal projection of the thrust-slip vector (arrows on thrust faults) and the strike-normal vector, and the stress ratio σ_s/σ_z are computed (Eqs. 3, 5, and 8) assuming constant values of R = 0.7 and μ_s/μ_t = 0.6, and the strikes and dips of the faults shown.

REFERENCES AND NOTES

1. W. R. Lettis and K. L. Hanson, *Geology* **19**, 559 (1991).
2. A. J. Michael, *Geophys. Res. Lett.* **17**, 1453 (1990).
3. T. J. Fitch, *J. Geophys. Res.* **77**, 4432 (1972).
4. J. Pacheco and J. Nabelek, *Bull. Seismol. Soc. Am.* **78**, 1907 (1988).
5. C. Nicholson, H. Kanamori, C. R. Allen, *Eos* **68**, 1362 (1987).

6. J. P. Eaton, *U.S. Geol. Surv. Prof. Pap. 1487*, 113 (1990); G. L. Choy, *ibid.*, p. 193; S. A. Sipken and R. E. Needham, *ibid.*, p. 193; H. Kanamori, *Calif. Div. Mines Geol. Spec. Publ.* **66**, 233 (1983); S. A. Sipkin, *J. Geophys. Res.* **91**, 531 (1986); D. Eberhart-Phillips, *ibid.* **94**, 15565 (1989).
7. H. Kanamori and K. Satake, *Geophys. Res. Lett.* **17**, 1179 (1990); G. L. Choy and J. Boatwright, *ibid.*, p. 1183; L. J. Ruff and B. W. Tichelaar, *ibid.*, p. 1187; B. Romanowicz and H. Lyon-Caen, *ibid.*, p. 1191; J. Zhang and T. Lay, *ibid.*, p. 1195.
8. M. E. Beck, Jr., in *Paleomagnetic Rotations and Continental Deformation*, C. Kissel and C. Laj, Eds. (Kluwer, Boston, 1989), p. 1; *Phys. Earth Planet. Inter.* **68**, 1 (1991).
9. Neither model here is identical to Beck's formulation (*8*), which holds that the plate velocity and its azimuth are the same far from and in the thrust. This effectively is bending the plate about a horizontal axis orthogonal to the plate motion rather than bending the plate about the strike of the thrust. R. McCaffrey, *J. Geophys. Res.*, in press.
10. The last two terms of Eq. 1 are important if determining the optimal dip of the thrust fault. Ignoring them results in the incorrect conclusion that the optimal dip for the thrust is 90° (*2*).
11. Alternatively we can express ψ in terms of R and Δ: $\sin\psi = R(\cot^2\Delta + R^2 \sin^2\Delta)^{-1/2}$
12. Alternatively, $\tan\phi = [-1 \pm (1 + 4S(1 - S)\tan^2\zeta)^{1/2}]/2\tan\zeta\,(1 - S)$ when $S \neq 1$ and $\theta = \zeta$ when $S = 1$.
13. The ratio works out to $\tau_s/\tau_t = [\sin^2\Delta + \sin^2 2\Delta\,(\sin^2\phi - S)^2/\sin^2 2\phi]^{-1/2}$, which reduces to R using Eq. 6.
14. W. F. Brace and D. L. Kohlstedt, *J. Geophys. Res.* **85**, 6248 (1980).
15. V. S. Mount and J. Suppe, *Geology* **15**, 1143 (1987).
16. Working Group on California Earthquake Probabilities, *U.S. Geol. Surv. Circ.* **1053** (1990).
17. C. P. Prentice, thesis, California Institute of Technology (1990).
18. C. DeMets, R. G. Gordon, D. F. Argus, S. Stein, *Geophys. J. Int.* **101**, 425 (1990).
19. M. Lisowski, W. H. Prescott, J. C. Savage, M. J. Johnston, *Geophys. Res. Lett.* **17**, 1437 (1990).
20. R. S. Stein, G. C. P. King, J. B. Rundle, *J. Geophys. Res.* **93**, 13319 (1988).
21. G. Valensise and S. N. Ward, *Bull. Seismol. Soc. Am.* **81**, 1694 (1991).
22. R. D. Burford and P. W. Harsh, *ibid.* **70**, 1233 (1980); K. E. Sieh and R. H. Jahns, *Geol. Soc. Am. Bull.* **95**, 883 (1984).
23. R. S. Stein and R. S. Yeats, *Sci. Am.* **260**, 48 (1989).
24. R. J. Weldon and K. E. Sieh, *Geol. Soc. Am. Bull.* **96**, 793 (1985).
25. C. R. Allen, *Bull. Geol. Soc. Am.* **68**, 315 (1957).
26. J. C. Matti, D. M. Morton, B. F. Cox, *U.S. Geol. Surv. Open-File Rep.* **85-365** (1985).
27. We thank the National Science Foundation for supporting this research through NSF grants EAR-8915833 and EAR-9005092. Center for Neotectonic Studies Contribution Number 6.

8 November 1991; accepted 18 February 1992

Rejection of the "Flying Primate" Hypothesis by Phylogenetic Evidence from the ϵ-Globin Gene

Wendy J. Bailey, Jerry L. Slightom, Morris Goodman

Whether the bat suborder Megachiroptera (megabats) is most closely related to the other suborder of bats, Microchiroptera (microbats), or whether Megachiroptera is the sister group of order Primates has been an issue of much debate. Should all bats be classified into a monophyletic order (Chiroptera) or do bats have diphyletic origins, and are the megabats actually "flying primates"? These questions were addressed by phylogenetic analysis of ϵ-globin gene sequences from a number of primates and other eutherian mammals. Results of parsimony analysis not only support bat monophyly, but the strength of Chiroptera grouping is comparable to that supporting the monophyly of the prosimian primate suborder Strepsirhini (galago and lemur). Furthermore, 39 derived nucleotide sequence changes are uniquely shared by the megabat (*Cynopterus sphinx*) and microbat (*Megaderma lyra*) versus three commonly shared by the megabat, primates, and Dermoptera or flying lemur (*Cynocephalus variegatus*), and only two shared by either megabat and primates, or by megabat and flying lemur.

Debate over chiropteran origins began as early as the 1700s when Linnaeus (*1*) first placed the bats with the order Primates in mammalian taxonomy. The classical hypothesis (*2*)—a monophyletic grouping of megabats, suborder Megachiroptera, with microbats, suborder Microchiroptera, in order Chiroptera—is based on an array of morphological traits including common wing structure, cranial vascular features, and fetal membranes (*3*). Furthermore, Novacek proposed that Dermoptera (flying lemur) and Chiroptera are most closely related to each other and that they should be included in a superorder Archonta with Primates and Scandentia (tree shrews) (*4*).

In contrast, the diphyly of bats or "flying primate" hypothesis advocates that flight evolved twice in mammals, once in the early descent of Microchiroptera, and again later in the lineage leading to the Megachiroptera from a common lineage shared with Primates and Dermoptera (*5*, *6*). Pettigrew's analysis of neural anatomy in the visual and motor pathways led him to conclude that the brains of Primates, Dermoptera, and Megachiroptera share important derived features that are absent in Microchiroptera (*5*, *7*). Additional evidence for the diphyly of bats is the presence of a glans penis, found only in Dermoptera, Megachiroptera, and Primates (*8*).

Elucidating the true phylogeny of Chiroptera has relevance to the origins of Primates, Dermoptera, and Scandentia. It also provides a framework for exploring evolutionary processes, because both megabats and microbats share similar wing structures, whereas megabats and primates share similar neural pathways. Thus, one set of these shared traits represents homoplasy (superficial similarity due to convergence or reversal). Morphological evidence has failed to define accurate phylogenetic relationships between megabats, microbats, and other eutherian mammals (*3*, *6*, *7*).

The evidence on bat origins from earlier molecular studies have been inconclusive as well (*9*, *10*). In seeking more definitive molecular evidence, we have analyzed a data set of DNA sequences representing the ϵ-globin gene from 11 primates, flying lemur, tree shrew, megabat, microbat, rabbit, and goat. Our study provides molecular evidence from a nuclear gene directed at answering whether megabats share a more recent common ancestor with primates or microbats.

The ϵ-globin gene in mammals is the 5′-most member of the β-globin gene cluster that arose from a series of tandem duplications, the first of which occurred about 200 million years ago (Ma) and led to the embryonically expressed proto-ϵ gene and the postnatally expressed proto-β gene. By the time of the first placental mammals (90 to 100 Ma), further tandem duplications resulted in five gene loci linked in the order 5′-ϵ-γ-η-δ-β-3′ (*11*). In placental mammals, the ϵ gene has been much less prone to undergo further tandem duplications than have the other β-type globin genes. Therefore, it is well suited for the study of phylogenetic relationships because the problem of comparing paralogous genes (genes derived from duplication events) is largely avoided. In addition, the majority of the sequence data is noncoding, hence it is not under selective constraints that may result in functional homoplasies.

Sequence analysis encompassed 17 orthologous genes (genes derived from speciation events). The data set consisted of sequences from previously published data, lambda library subclones, and polymerase chain reaction (PCR)–generated clones

W. J. Bailey, Department of Molecular Biology and Genetics, Wayne State University School of Medicine, Detroit, MI 48201.
J. L. Slightom, Department of Anatomy and Cell Biology, Wayne State University School of Medicine, Detroit, MI 48201, and Molecular Biology Unit 7242, The Upjohn Company, Kalamazoo, MI 49007.
M. Goodman, Department of Anatomy and Cell Biology and Department of Molecular Biology and Genetics, Wayne State University School of Medicine, Detroit, MI 48206.